Rock Mechanics and Rock Engineering (2023) 56:2137–2156
https://doi.org/10.1007/s00603-022-03125-x

ORIGINAL PAPER

Experimental Study on Shear-Seepage Coupling Characteristics of Single Fractured Rock Mass Under Cyclic Loading and Unloading

Tianjiao Yang[1] · Pengyu Wang[2] · Shuhong Wang[3] · Huan Liu[3] · Ze Zhang[3]

Received: 29 January 2022 / Accepted: 21 October 2022 / Published online: 28 November 2022

Abstract

To reveal the shear-seepage coupling characteristics of fractured specimens under cyclic loading and unloading, the specific test device and test method were designed in this study. The cyclic loading and unloading shear-seepage coupling test on the fractured rock mass under different confining pressures and seepage pressures was carried out by processing "double L-shaped" specimens, and the change laws of the shear characteristics and seepage characteristics of fractured specimens with different roughness were experimentally investigated. The results indicated that the peak shear stress, residual shear stress, and shear stiffness of rough fractures all increase with increasing confining pressure, while the change in normal dilatation displacement is the opposite. Under a constant normal stress, the permeability of rough fracture decreases, increase, and then stabilizes with increasing shear displacement. The peak shear stress of the smooth fracture is 3.7 times lower than that of the rough fracture with the same shear displacement, and the smooth sandstone specimens are all in a shear shrinkage state, with the normal shrinkage displacement of less than 1.0 mm. In addition, during unloading, permeability increases to some extent but cannot recover to the original value. The confining pressure causes permanent damage to the permeability of fractured rock mass. The permeability of sandstone specimens changes primarily in the early loading stage and late unloading stage. Based on the test results, the relationship between permeability and confining pressure follows a negative exponential function under cyclic loading and unloading conditions.

Highlights

- The shear-seepage coupling test device and test method were designed.
- The effect of seepage pressure on the hydro-mechanical coupling of rough fractures has a threshold value.
- The permeability of rough fractured specimen changes in the staged manner of "decrease-increase-stability" with increasing shear displacement.
- The initial stage of loading and the later stage of unloading are the main stages of permeability change of fractured sandstone specimens.

Keywords Cyclic loading and unloading · Single fractured rock mass · Shear-seepage coupling · Permeability · Confining pressure

✉ Pengyu Wang
wangpengyu6666@126.com

Tianjiao Yang
yangtianjiaols@126.com

Shuhong Wang
shwang@mail.neu.edu.cn

Huan Liu
lh_advance@126.com

Ze Zhang
zhangze210@126.com

[1] School of Physical and Mathematical Sciences, Nanjing Tech University, Nanjing 211816, Jiangsu, China

[2] College of Transportation Engineering, Nanjing Tech University, Nanjing 211816, Jiangsu, China

[3] Department of Resources and Civil Engineering, Northeastern University, Shenyang 110819, China

1 Introduction

Excavating an engineering rock mass results in a large number of mining-induced fractures (Fu et al. 2021; Kong et al. 2021; Li et al. 2021), which weaken the overall mechanical properties of rock mass (Vazaios et al. 2019; Liu et al. 2021) as well as affect the permeability characteristics of rock mass (Chen et al. 2016; Aalianvari et al. 2017; Xue et al. 2019). During tunnel excavation, tunnel surrounding rock will undergo shear slip (Guo et al. 2019; Abierdi et al. 2020; Chen et al. 2020). In shear failure and even rock mass instability, the potential shear fracture surface is under normal unloading conditions (Li et al. 2015, 2020; Jia et al. 2021). Compared with intact rock, the mechanical and hydraulic properties of fractured rock mass are significantly different under loading and unloading conditions (Huang et al. 2020; Ren et al. 2020; Xiang et al. 2021). For fractured rock mass, a single fracture is the basic unit that constitutes the fracture network of rock mass, and the study of its mechanical and hydraulic coupling characteristics is the basis of more complex coupling behavior of a fractured rock mass (Di et al. 2017; Sun et al. 2019; Tian et al. 2021; Yang et al. 2021; Zhang et al. 2021a). Therefore, analyzing the shear-seepage coupling characteristics of a single fractured rock mass under cyclic loading and unloading conditions is significant for improving engineering excavation methods.

Different scholars have developed different types of shear-seepage test devices (Zhang et al. 2019; Shen et al. 2021) and carried out experimental studies on the shear-seepage characteristics of fractures caused by factors such as fluid injection mode (Yeo et al. 1998; Wang et al. 2020a), normal loading mode (Chen et al. 2000; Chao et al. 2020), normal stress magnitude (Cao et al. 2018; Wang et al. 2020b), and fracture roughness (Nishiyama et al. 2014; Huang et al. 2017; Qian et al. 2018; Liu et al. 2020a). As for the shear-seepage test fluid injection mode, most scholars adopt unidirectional flow (Lee et al. 2002; Javadi et al. 2014), that is, the fluid is injected along the end of the specimen and the flow direction is the same as the shear direction. This method is widely used, the shear displacement of specimens is large, and cubic law can be used to easily calculate the hydraulic opening; however, determining the fluid sealing during shearing is difficult. At present, the study of normal loading mode primarily focuses on a constant normal stress and constant normal stiffness (Ahola et al. 1996). Esaki et al. conducted shear-seepage tests on granite structural planes under constant normal stress conditions and found that the hydraulic conductivity of fractures increased by an order of magnitude after shearing (Esaki et al. 1999), and there are many similar loading methods (Rong et al. 2016). Many scholars have used self-developed test devices to discuss the influence of normal stress, shear displacement, and seepage pressure on the seepage law of fractures (Olsson and Barton 2001; Park et al. 2013; Yin et al. 2017). These test specimens are primarily square specimens, and the maximum normal stress and shear displacement can reach 60 MPa and 20 mm, respectively, but due to a lack of proper sealing around the shear box, the maximum seepage pressure that can be applied in the test can reach 0.6−1 MPa. In addition, the damage of the fracture surface (Boulon et al. 1993; Liu et al. 2016), accumulation of filling material (Koyama et al. 2009; Vogler et al. 2016), and evolution of the geometric characteristics of the fracture surface (Xiong et al. 2011; Gui et al. 2017; Mofakham et al. 2018; Li et al. 2019) are the roughness mechanisms affecting the shear-seepage coupling characteristics (Rong et al. 2018).

The stress paths for rock mass unloading and loading are completely different, leading to different strengths, deformation, failure mechanisms, and permeability characteristics (Qiu et al. 2014; Meng et al. 2016, 2018; Zhu et al. 2019; Gramiger et al. 2020; Liu et al. 2020b; Zhang et al. 2021b; Zhao et al. 2021a; Zhao et al. 2022). In addition, the effect of unloading on rock mass mechanical and hydraulic properties cannot be ignored (Zhou and Shou 2013; Duan et al. 2019; Feng et al. 2020; Peguiron and Labiouse 2020; Jiang et al. 2020; Zhao et al. 2021b). Zhang et al. (2020) carried out hydro-mechanical coupling tests on fractured sandstone specimens under cyclic loading and unloading, and proposed the concept of the permeability recovery rate (PRR) and permeability enhancement reduction rate (PERR) to characterize the change of permeability. The results show that the PERR of single fractured sandstone increases, while the cumulative PRR fluctuates in a "*V*" shape. In addition, numerous scholars have conducted experimental studies on the permeability characteristics of different types of rock fractures under cyclic loading and unloading (Cappa et al. 2005, 2006; Sathar et al. 2012; Faoro et al. 2013; Kling et al. 2016; Zhang et al. 2018; Ma et al. 2019; Eggertsson et al. 2020; Zhang et al. 2021c).

The current experimental research on the mechanical and hydraulic coupling characteristics of a single fracture has the following shortcomings: (1) it is difficult to ensure the sealing of fluid during the shear test, making it impossible to analyze the effect of high seepage pressure on the shear characteristics of fractures. (2) The behavior of rock mass deformation and permeability is very different under unloading and loading conditions. However, there are relatively few experimental studies analyzing the shear-seepage coupling characteristics under cyclic loading and unloading conditions. In this paper, sandstone specimens with a single fracture are analyzed. Shear-seepage coupling tests of a rock mass with single fracture under cyclic loading and unloading were carried out using topographic scanning and an independently designed shear-seepage coupling test method. Also, the mechanical and hydraulic coupling characteristics

of smooth and rough fractures were studied. The changes in mechanical and hydraulic parameters after cyclic loading and unloading of fractured rock mass studied in this paper are of great significance for underground rock mass excavation methods.

2 Experimental Method

In underground engineering, such as tunnel excavation and deep coal seam mining, in fact, the fractured rock mass is subjected to the joint action of seepage, cyclic loading and unloading in the process of excavation. During loading, the fracture surface still has good mechanical properties; however, its mechanical characteristics deteriorated significantly during unloading. At the same time, the physical properties of rock mass, such as strength characteristics and permeability, will change obviously during cyclic loading and unloading process. Based on this, the study of shear-seepage coupling characteristics of fractured rock mass under cyclic loading and unloading conditions has important significance and scientific value for the prevention and control of water inrush and mud inrush in the process of underground engineering excavation. Therefore, this paper carried out shear-seepage tests on single fractured sandstone under cyclic loading and unloading to study the seepage and shear characteristics of single fractured rock mass under mechanical and hydraulic coupling.

2.1 Experimental Setup

The experiment was carried out using a multi-field coupled triaxial apparatus. The test system was manufactured by Top Industry in France (Fig. 1).

The system consists of six parts: control system, triaxial pressure chamber, axial pressure system, confining pressure system, seepage system, temperature system, and special high-precision sensors (displacement, pressure, temperature). The triaxial pressure chamber is used to install special shear test specimens, as shown in Fig. 1c. For this experiment, the axial pressure provides the shear pressure in the test, and the confining pressure provides the normal stress in the test. The seepage pressure is applied using an injection pump, and the seepage pressure should be less than the confining pressure to avoid fluid flow from the gap between the specimen and the rubber jacket.

2.2 Specimen Preparation and Measurement of Morphological Parameters

The system focuses on sealing the test specimens. In this paper, the method of reforming the shear-seepage coupling test system for single fractured rock mass is achieved by analyzing specific "double L shaped" specimens. First, a single fractured sandstone specimen with a size of Φ50*100 was prepared using a Brazilian splitting device (Fig. 2a). Then, the same length l = 10 mm at the opposite ends of the upper and lower blocks were cut (Fig. 2b). An "*L* shaped" hole with an aperture of 3 mm and a hole depth of (l + 3) mm was drilled on the opposite face without cutting, and the other end of the hole exited the fracture surface (Fig. 2c). Then, A VTOP 300 T scanner was used for 3D morphology scanning of the fracture surface (Fig. 2d). Finally, the two rock masses were assembled and placed in a mold with an inner diameter of 50 mm, and liquid silicone rubber was used to evenly fill the part of the end face of the cut rock to restore the specimen to its original shape (Fig. 2e). The filled mold was left for 48 h, and the mold was opened after the silicone rubber was fully solidified (Fig. 2f). To reduce seepage time, each sandstone specimen was vacuum-saturated before the test (Fig. 2g). Once the preparation of the "double-L-shaped" specimens was completed, each specimen was placed in the triaxial chamber (Fig. 2h). Next, the confining pressure, axial shear force, and seepage pressure were loaded to carry out the shear-seepage test under cyclic loading and unloading conditions.

Sixteen specimens of bluish sandstone were selected in this test (Fig. 3). To ensure accuracy of the experiment, the roughness of the structural plane is approximately equal to one group. The formula for calculating the joint roughness coefficient (JRC) is as follows (Tse and Cruden 1979; Jang et al. 2014; Zhao et al. 2018):

$$\mathrm{JRC} = 32.2 + 32.47 \log Z_2 \tag{1}$$

$$Z_2 = \left[\frac{1}{L}\int_{x=0}^{x=L}\left(\frac{\mathrm{d}y}{\mathrm{d}x}\right)^2 \mathrm{d}x\right]^{1/2} = \left[\frac{1}{L}\sum_{i=1}^{n-1}\frac{\left(y_{i+1}-y_i\right)^2}{x_{i+1}-x_i}\right]^{1/2} \tag{2}$$

where Z_2 is the root mean square of the first derivative; y_i is the height of the joint profile x_i,Δx is the distance between x_{i+1}, and x_i, L is the horizontal length of the joint profile.

To analyze the mechanical and hydraulic coupling characteristics of rough fractures, specimens S13 and S14 in comparison group 3 were not subjected to seepage pressure. In addition, to study the effect of fracture roughness on the test results, a comparative test was added. Artificial fractures (specimens S15 and S16) were machined in intact specimens of the same size with a high-precision chainsaw, and the roughness of the two specimens was very small. The

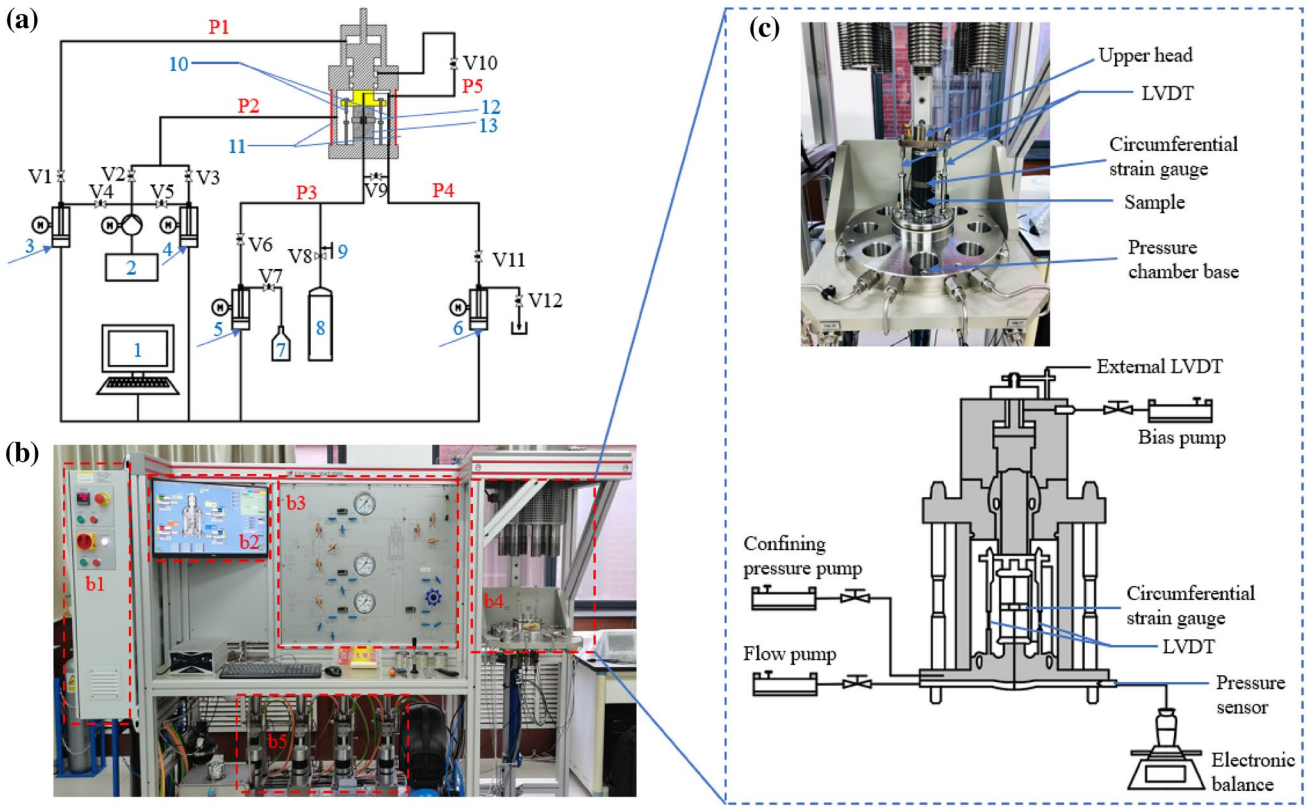

Fig. 1 Multi-field coupled triaxial apparatus **a** Sketch of the triaxial system (P1—axial loading path; P2—confining pressure loading path; P3—upstream chamber seepage path; P4—downstream chamber seepage path; P5—self-balancing system; V1–V12—switch; 1—computerized data-acquisition unit; 2—fuel reservoir; 3–6—high-precision flow pump; 7—water reservoir; 8—high-pressure gas; 9—pressure relief valve; 10—LVDT; 11—electric heating ring; 12—circumferential strain gauge; 13—specimen); **b** picture of the testing system (b1—system host; b2—main system control display panel; b3—system valve operation panel; b4—triaxial pressure chamber; b5—pressure pump, from left to right: axial pressure pump, confining pressure pump, upstream water pressure pump, downstream water pressure pump); **c** Detail picture of the triaxial pressure chamber

dimensions, roughness coefficients, and test conditions of all the specimens are listed in Table 1. All specimens in this test were processed using the test steps outlined above (Fig. 2). The pre-cast length of silicone rubber for each specimen was 10 mm, and the preset shear length was 8 mm.

2.3 Experimental Procedure

The specific steps of the shear-seepage coupling test of single fractured rock mass under cyclic loading and unloading conditions are as follows:

(1) Scanning of fracture surface topography. To observe the failure of the fracture surface bulge caused by stress loading and fluid flow, the point cloud of the fracture surface was first processed (Fig. 4i, v) and digitally characterized (Fig. 4ii, vi). Next, two-dimensional topography (Fig. 4iii, vii) and three-dimensional topography (Fig. 4iv, viii) of the fracture surface were generated using MATLAB.

(2) The preparation and sealing of the specimens are shown in Fig. 2.

(3) Shear-seepage coupling test under cyclic loading and unloading conditions. First, the confining pressure was increased to the test value and held for 5 min until the pressure stabilized. Then, the liquid injection pump was turned on to increase the seepage pressure within the fracture, the injection pump was closed, the axial loading cylinder was opened, and shear displacement loading was carried out at a constant rate of 0.002 mm/s. When the test increased to a selected shear displacement, the loading cylinder was suspended, the injection pump was opened, and the injection seepage pressure was increased into the fracture in stages, which is about 7–8 groups. The maximum injected seepage pressure should not be greater than the confining pressure. The

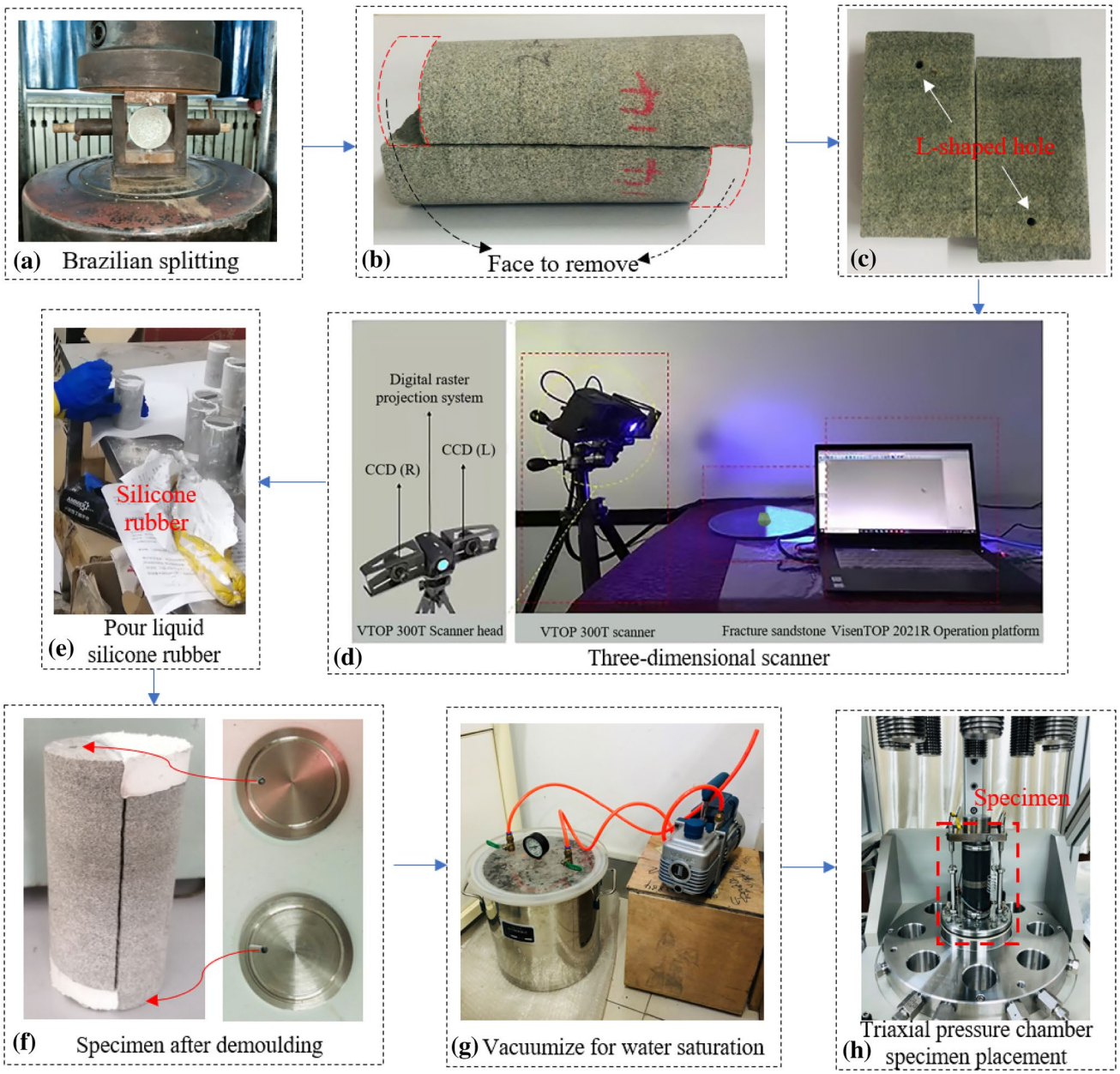

Fig. 2 Preparation flow chart of "double-L-shaped" specimens

next set of seepage tests can be carried out only when the seepage tests at each stage are stable. After completing all the seepage tests, the injection pump was closed, the axial loading cylinder was reopened, and the shear displacement was continuously applied. The above seepage test steps were repeated when the shear displacement increased to the selected shear displacement for the next stage. According to this, the seepage test for grade 7–8 shear displacement was carried out, and the injection pump was shut down after all the seepage tests were completed. The ideal shear length of the test is equal to the length of silicone rubber (10 mm) filled by the end face of the specimen. If leakage occurred along the side of the fracture during the test, the test was stopped. Finally, cyclic loading and unloading tests were carried out in stress control mode with a constant shear stress and seepage pressure. Axial deformation, radial deformation, pressure changes, and flow changes were monitored synchronously throughout the test.

Fig. 3 Appearance of bluish sandstone specimen

3 Results and Discussion

3.1 Hydraulic Characteristics Analysis of Fractured Sandstone Under Normal Loading

The variation curves of flow rate, permeability, axial, and radial deformation of the specimen with increasing seepage pressure under constant confining pressure are shown in Fig. 5. When the seepage pressure increases from 0 to 2.2 MPa, the axial and radial deformations of the specimen slowly increase in a "step-like" manner, with an increase of about 14.95E-2 mm and 14.98E-2 mm, respectively, but the permeability and hydraulic opening remain unchanged at 5.27E-9 m^2 and 25.15E-2 mm, respectively (Fig. 5a). The unequal relationship between fracture mechanical deformation and hydraulic opening is related to fracture roughness. When the seepage pressure increases from 2.2 to 3 MPa, the axial and radial deformations increase linearly, the fracture permeability increases suddenly, and the mechanical and hydraulic coupling effect is significant. When the seepage pressure increases from 0 MPa to about 2.7 MPa, the axial and radial deformation of the specimen increase by 11.20E-2 mm and 11.17E-2 mm, respectively (Fig. 5b). Simultaneously, the flow rate increases slowly, and the permeability decreases from 4.03 to 3.87E-9 m^2, primarily because the fracture produces non-Darcy flow characteristics, which means the increasing seepage pressure per unit increment does not cause an equal increase of flow rate. When seepage pressure increases from 2.7 to 4 MPa, the fracture deformation, flow rate, and hydraulic opening increase with increasing seepage pressure, and the mechanical and hydraulic coupling effect of fracture is significant. When the confining pressure is constant, the influence of seepage pressure on the mechanical and hydraulic coupling of rough fractures has a certain critical range. When the seepage pressure is lower than this range, the coupling characteristics are not significant; when it is within this range, the coupling characteristics are significant.

In addition, the flow rate increases with increasing seepage pressure under different confining pressure conditions, but there are significant differences in the variation law of the curve growth (Fig. 5). When the confining pressure is 24 MPa, the flow rate with increasing seepage pressure can be fit using an exponential function. When confining pressure reaches 30 MPa, the curve of flow rate and seepage pressure shows a significant turning point. When the seepage pressure is less than 2.7 MPa, the flow rate increases linearly with seepage pressure, but the growth rate is very low. When the seepage pressure is greater than 2.7 MPa, it also shows a linear increase, but the slope changes significantly, and the growth rate increases significantly. The data can be fit using a bilinear function with the turning point as the boundary.

The variation curve of permeability of different fracture specimens with confining pressure is shown in Fig. 6. With increasing confining pressure, the permeability of the specimen gradually decreases (Fig. 6a). In general, the permeability decreases rapidly at the beginning, but with increasing confining pressure, permeability decreases gradually. The above studies show that when the confining pressure is small, the smaller contact part of the two rough fracture surfaces is compressed, and the fracture rapidly produces large deformation and permeability decreases rapidly. With increasing stress, the contact area of the two compressed rough fracture surfaces of the specimen becomes larger and larger, so that the deformation capacity of the fracture gradually decreases, and the permeability gradually decreases gradually. Under the same confining pressure, the permeability of the fracture decreases with decreasing seepage pressure (Fig. 6b).

3.2 Shear-Seepage Coupling Characteristics Analysis of Fractured Sandstone Under Normal Loading

3.2.1 Relations Between Shear Stress and Shear Displacement

Rough fractures exhibit complex mechanical properties during shearing. The shear stress curve and shear characteristic parameters of the fractured sandstone are shown in Fig. 7 and Table 2, respectively.

Table 1 Dimensions, roughness coefficients, and test conditions of all the specimens

Specimen type	Specimen status	Group 1	Shear displacement loading rate (mm/s)	JRC	Specimen length (mm)	Specimen diameter (mm)	Seepage pressure difference (MPa)	The confining pressure value of the first load (MPa)	The confining pressure value of cyclic unloading (MPa)	The confining pressure value of cyclic loading (MPa)
Bluish sandstone	Saturated	S1	None	8.4166	100.04	50.61	2.5	30	15	30
		S2		8.3087	101.32	50.32	2.5	28	14	28
		S3		8.4239	99.46	49.38	2.5	26	13	26
							Confining pressure (MPa)	Seepage pressure difference (MPa)	Seepage pressure difference (MPa)	Seepage pressure difference (MPa)
		S4		8.2174	99.86	50.74	30	1	2.5	4
		S5		8.4959	100.08	50.22	24	1	2	3
		S6		8.4027	98.99	50.39	20	0.1	0.5	1
		Group 2	Shear displacement loading rate (mm/s)	JRC	Specimen length (mm)	Specimen diameter (mm)	Seepage pressure difference (MPa)	The confining pressure value of the first load (MPa)	The confining pressure value of cyclic unloading (MPa)	The confining pressure value of cyclic loading (MPa)
		S7	0.002	7.9401	99.83	50.11	2.5	30	15	30
		S8		7.7369	100.30	49.88	2.5	28	14	28
		S9		7.6397	99.78	49.83	2.5	26	13	26
							Confining pressure (MPa)	Seepage pressure difference (MPa)	Seepage pressure difference (MPa)	Seepage pressure difference (MPa)
		S10		7.8137	98.65	50.27	30	1	2.5	4
		S11		7.4244	101.23	49.14	24	1	2	3
		S12		7.8985	100.54	50.52	20	0.1	0.5	1
		Group 3 (Comparative group)	Shear displacement loading rate (mm/s)	JRC	Specimen length (mm)	Specimen diameter (mm)	Seepage pressure difference (MPa)	The confining pressure value of the first load (MPa)	The confining pressure value of cyclic unloading (MPa)	The confining pressure value of cyclic loading (MPa)
		S13	0.002	8.2456	99.76	49.65	0	28	14	28
		S14	0.002	7.8268	99.87	49.32	0	24	12	24
		S15	0.002	1.0994	100.10	49.93	2.5	28	14	28
		S16	0.002	1.8976	100.01	49.19	2.5	24	12	24

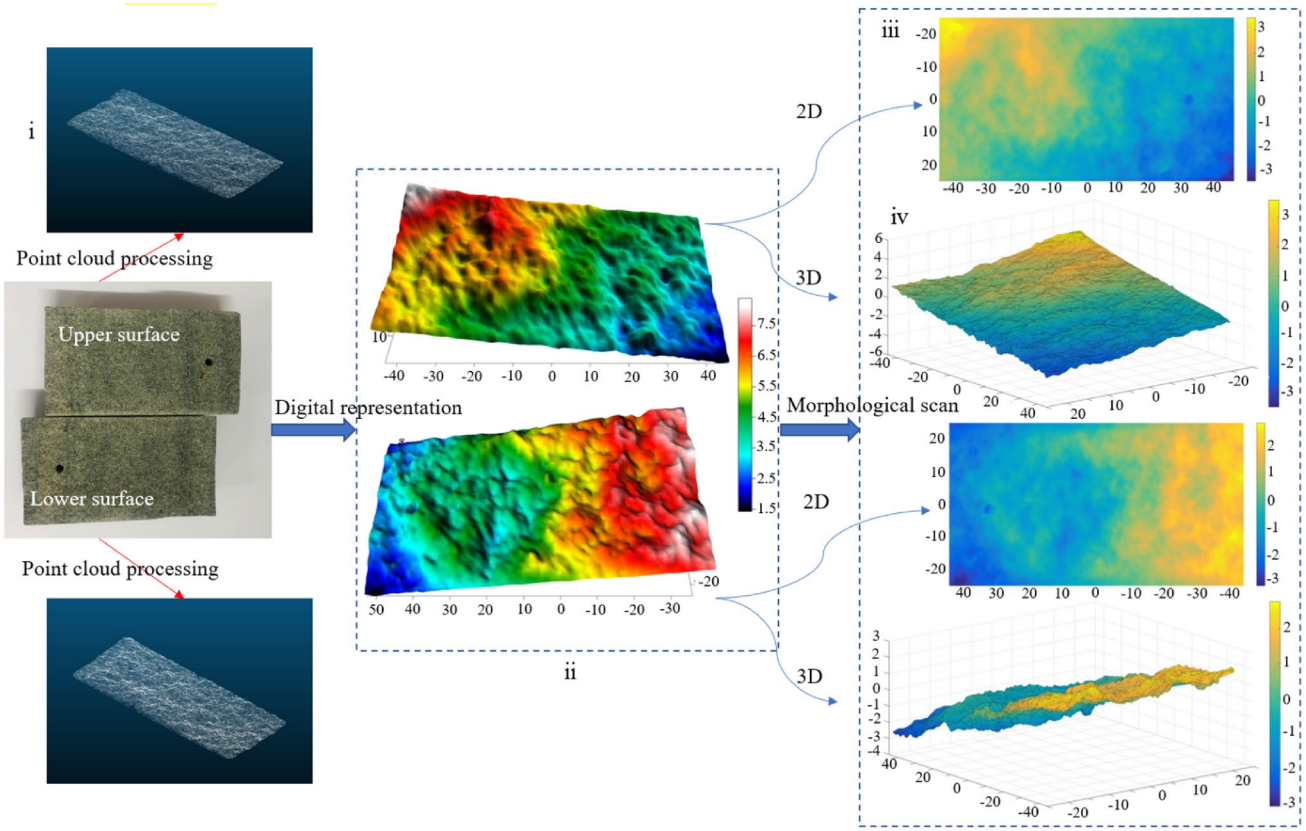

(a) rough fracture surface (specimen S7 as an example)

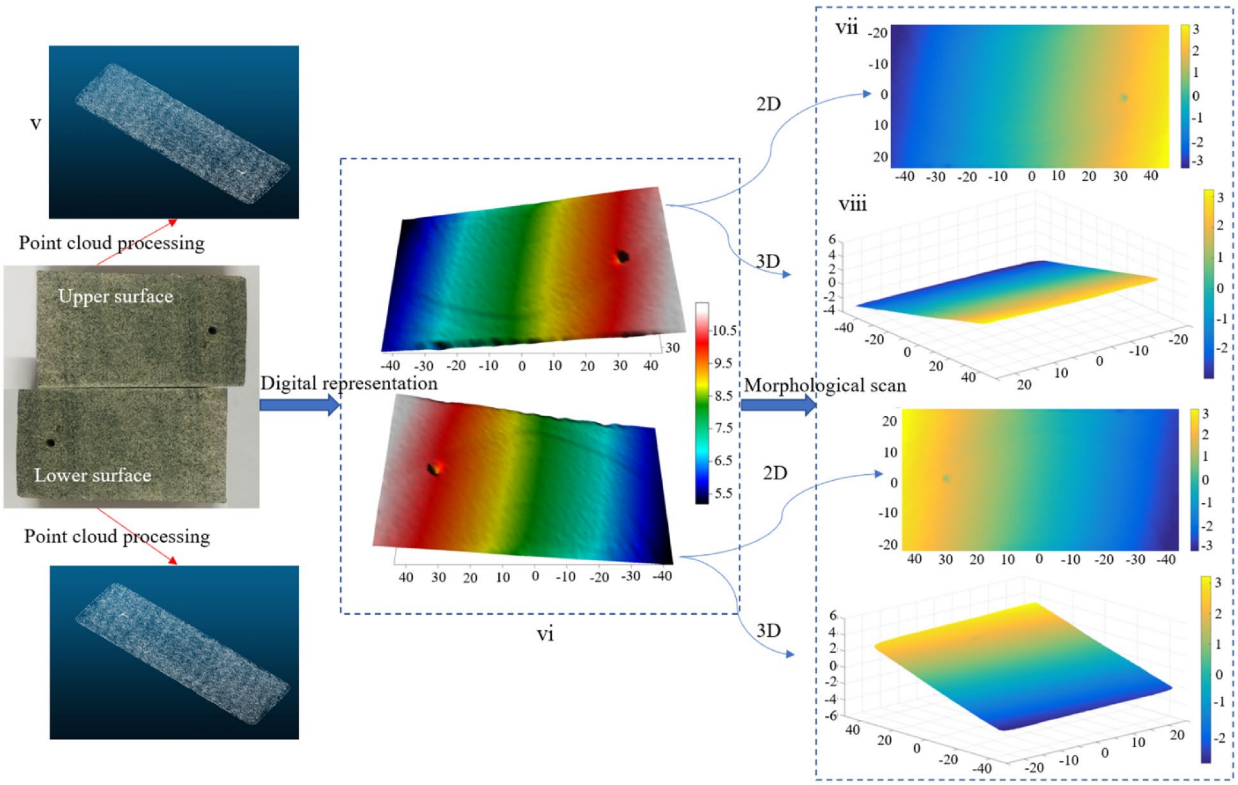

(b) smooth fracture surface (specimen S15 as an example)

Fig. 4 Morphology characterization of fracture surface

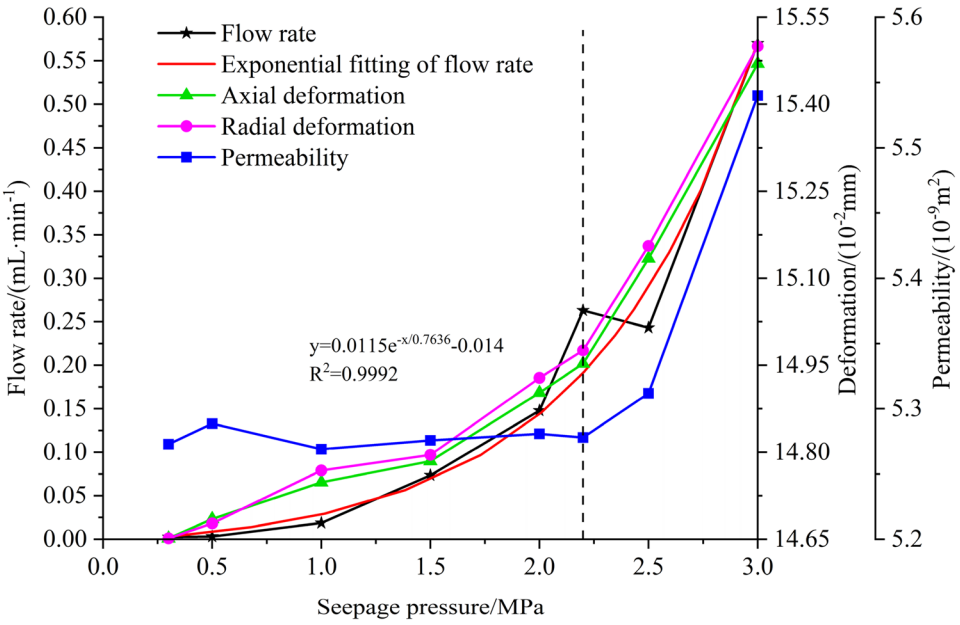

(a) Specimen S5 under a confining pressure of 24 MPa

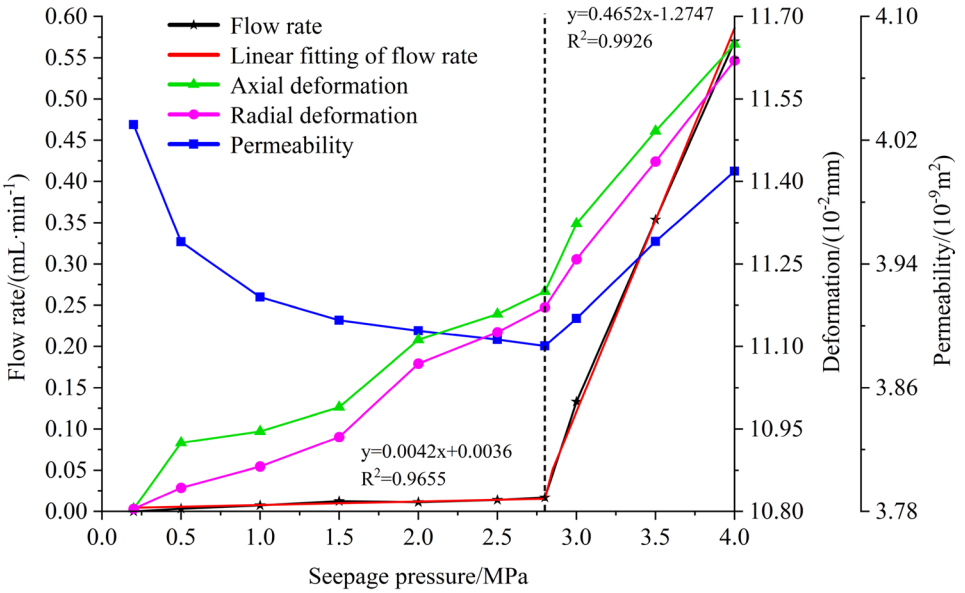

(b) Specimen S4 under a confining pressure of 30 MPa

Fig. 5 Variation curves of flow rate, permeability, axial, and radial deformation of the specimen with the seepage pressure under constant confining pressure

These curves generally show the following relationships (Fig. 7) when the shear displacement is initially loaded, ranging from 0 to 0.6 mm, the curves are all concave. Then, the curve increases linearly with increasing shear displacement, indicating that the fracture surface does not produce significant convex wear damage in this stage. Then, the shear stress almost linearly increases to the peak shear stress, and the corresponding shear displacement when it reaches the peak point is between 0.6 and 1.0 mm. Next, the shear stress decreased with increasing shear displacement, and most of the specimens attenuated sharply with a large decrease, which was due to the softening of the fracture surface as well as interactions with water, resulting in the weakening of and failure between particle bumps. However, some specimens attenuated slowly (S11 and S12) with a small decrease, and the difference in the decrease reflects the strength of the water–rock interaction. After the shear peak, the shear stress decreased to the residual shear stress in a form of almost negative exponential with increasing shear displacement. Finally, when the shear displacement reached 2–3.5 mm, the shear stress gradually stabilized, primarily due to the large failure area

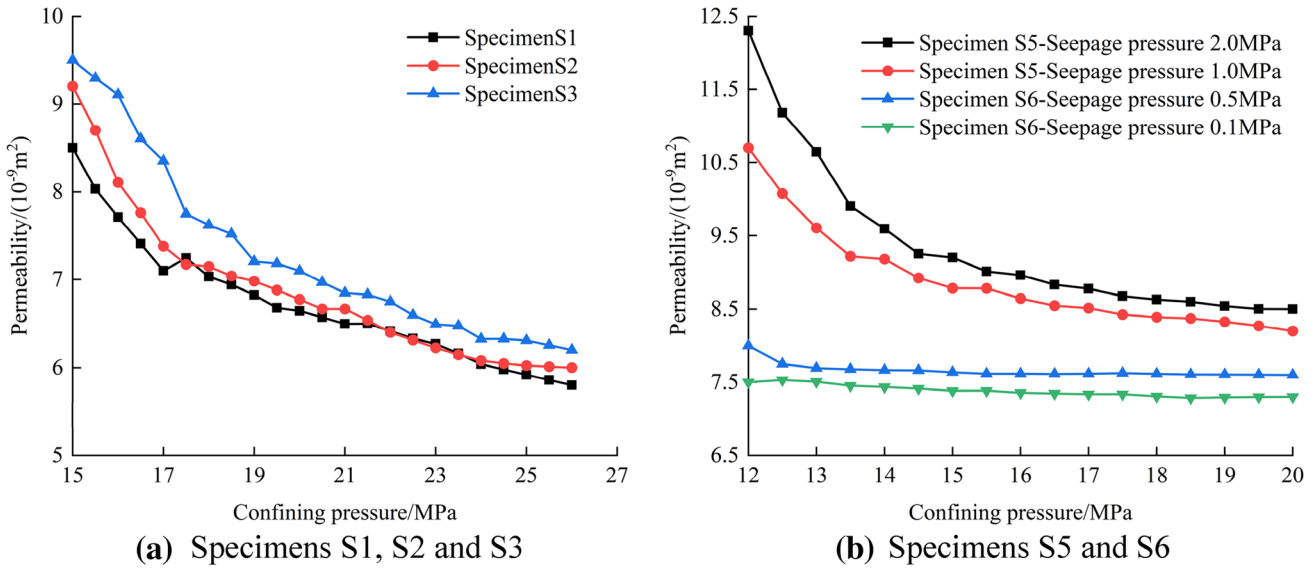

Fig. 6 Variation curve of permeability of fractured sandstones with confining pressure

between the protrusions where the fracture planes occlude each other.

In addition, the shear stiffness of the fracture increases significantly with increasing confining pressure (Fig. 7) (Table 2). The peak shear stress and residual shear stress of the fracture increase simultaneously with increasing confining pressure. In addition, in different shear stages, the shear stress curve of the fractures will appear as a tooth-like drop, which may be caused by shear slip on the fracture caused by the seepage pressure injected into the fracture at this time, resulting in the attenuation of the bearing capacity of the fracture. However, the bearing capacity will gradually recover after the seepage pressure is removed.

The shear stress–shear displacement curve of the rough fractured sandstone without seepage pressure coupling is shown in Fig. 8. Both the peak shear stress and the residual shear stress increase with increasing confining pressure. In the initial displacement strengthening stage, a small compaction stage with small shear stiffness can be observed, and the length of compaction stage tends to be longer with increasing confining pressure. Compared to the rough surface with shear-seepage coupling, there is no shear stress drop due to the lack of seepage pressure.

The shear stress–shear displacement curve for smooth fractured sandstone is shown in Fig. 9. Different from the rough fractured sandstone, the shear stress increases rapidly as shearing begins and does not soften immediately after reaching the peak value but continues to fluctuate slowly within 1 MPa until the end of shearing. The peak shear stress of the smooth fractured sandstone is 3.7 times lower than that of the rough fractured sandstone for the same shear displacement, indicating that the damage degree of the smooth fractured sandstone is the least.

3.2.2 Relationship Between Normal Displacement and Shear Displacement

Deformation of the fracture during shearing will lead to increasing or decreasing the fracture opening, leading to a complex change law for fracture permeability. The normal displacement–shear displacement variation curve of the specimen with a rough fracture during the shearing process is shown in Fig. 10. At the initial stage of shearing, the fractures undergo weak compression deformation (shrinkage). The maximum shrinkage of fractures varies from − 0.002 to − 0.027 mm. Then, with increasing shear displacement, joint dilatancy behavior occurs. At this stage, the contact area of the fracture surface decreases and the normal displacement increases rapidly due to the shear climbing effect of the fracture surface. Then, when the shear displacement reaches 2–3 mm, the normal displacement of the fracture increases at a decreasing rate. Finally, the normal displacement gradually reaches a stable value. In addition, the curve of specimen S12 after peak does not gradually slow down but increases at a uniform rate. The main reason for the above differences is that during shearing of the fracture in this test, the shear surface of the fracture is gradually increasing, causing many particle bumps to not decrease with progressive shearing, and thus continue to climb, resulting in increasing normal displacement. In addition, the periodic fluctuation of normal displacement after peak is caused by hydraulic loading. The final normal displacement of fractures gradually decreases with increasing confining pressure. This is primarily because increasing confining pressure will

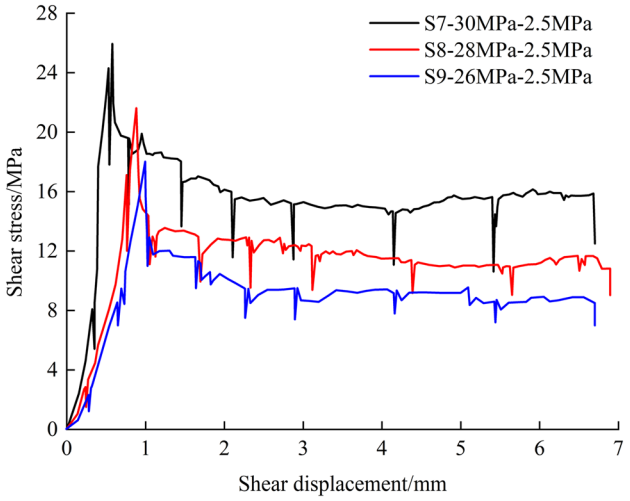

(a) Specimens S7, S8 and S9

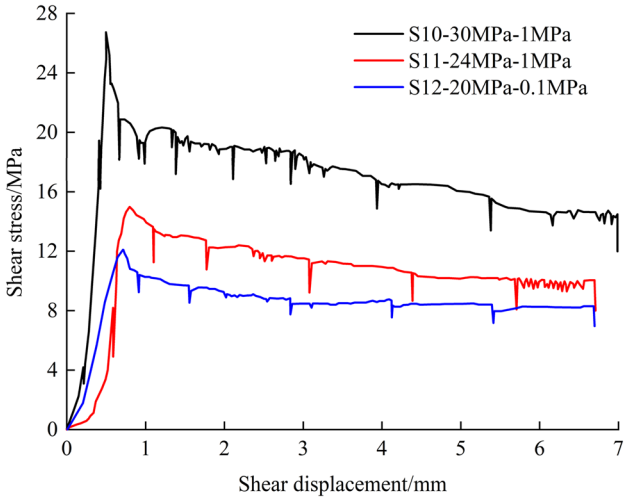

(b) Specimens S10, S11 and S12

Fig. 7 Relationship between shear stress and shear displacement for rough fractured sandstones (S7-30 MPa–2.5 MPa indicates that the confining pressure and seepage pressure of specimen S7 are 30 MPa and 2.5 MPa, respectively.)

restrict the normal deformation of fractures, which will reduce normal deformation. However, specimen S11 has the minimum normal displacement of 0.66 mm, which may be due to the smaller roughness value of specimen S11 compared to specimens S10 and S12.

The normal displacement–shear displacement curve of rough fractured sandstone without seepage pressure coupling is shown in Fig. 11. During shearing, normal deformation of fractures shows the phenomenon of shrinkage first followed by dilation. For the same fracture specimen, the final normal displacement of the fracture decreases with decreasing confining pressure. Compared with the rough surface with shear-seepage coupling, the deformation process is similar, but there is no periodic fluctuation in normal displacement at the later stage of shearing due to the absence of seepage pressure.

The normal displacement–shear displacement curve of the smooth fractured sandstone is shown in Fig. 12. Throughout the whole shearing process, all the specimens are in shear shrinkage state, with the normal shrinkage displacement of less than 1.0 mm. The initial shear section shows significant linear elastic deformation. With increasing shear displacement, the shear shrinkage section has a turning point, and the shear shrinkage slowly decreases. In addition, the greater the confining pressure, the more significant the shear shrinkage.

3.2.3 Effect of Shear Process on Seepage Characteristics

Shear slip of a rough fractured rock mass will cause dislocation and shear damage of the asperities between fracture surfaces and then cause a change in the fracture opening, affecting its seepage characteristics. This section primarily analyzes the seepage characteristics of fractures under different shear displacements.

At present, the parallel plate model with single fracture is the most widely used model in fracture seepage research, which qualitatively describes the relationship between fracture flow capacity and fracture width using the cubic law (Wu et al. 2018):

$$Q = \frac{b^3 w \Delta P}{12 \mu \Delta L} \tag{3}$$

where Q is the volume flow rate through the cross section of the specimen per unit time(m^3/s); b is the mechanical opening of the fracture(m);μ is the dynamic viscosity coefficient,

Table 2 Monitoring values of characteristic mechanical parameters of fractured sandstones during shear

Specimen	σ_t (MPa)	u_t^p (mm)	σ_t^p (MPa)	K_s (GPa / m)	u_t^r (mm)	σ_t^r (MPa)
S7	30	0.58	25.94	48.01	2.91	15.16
S8	28	0.88	21.62	25.04	2.05	12.76
S9	26	0.99	18.02	20.23	2.55	9.40
S10	30	0.50	26.73	52.53	3.08	17.24
S11	24	0.80	14.98	32.00	2.85	11.65
S12	20	0.71	12.10	26.67	2.53	8.78

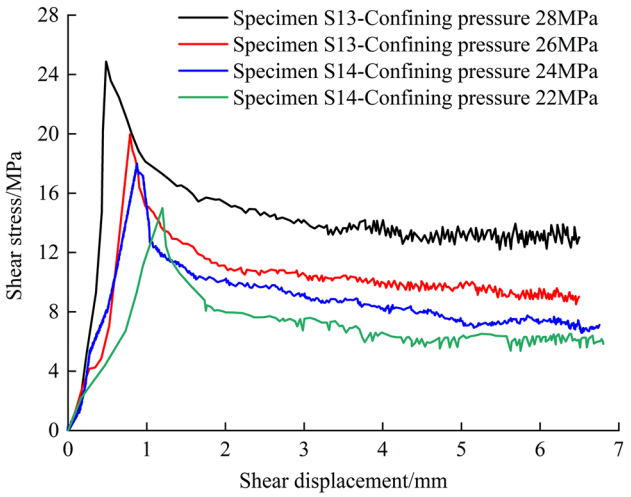

Fig. 8 Relationship between shear stress and shear displacement for rough fractured sandstones without seepage pressure coupling

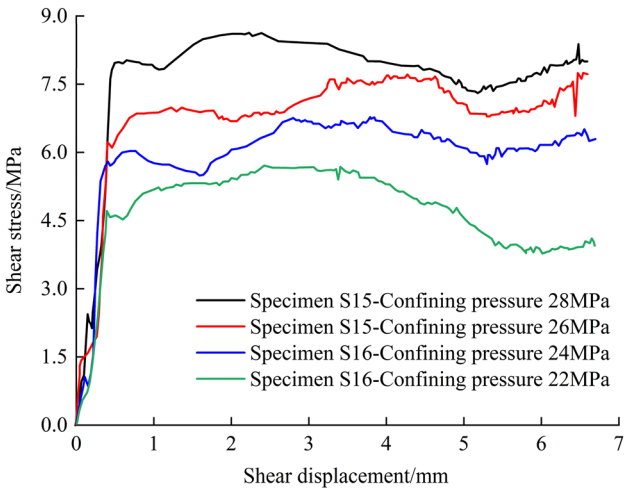

Fig. 9 Relationship between shear stress and shear displacement for smooth fractured sandstones

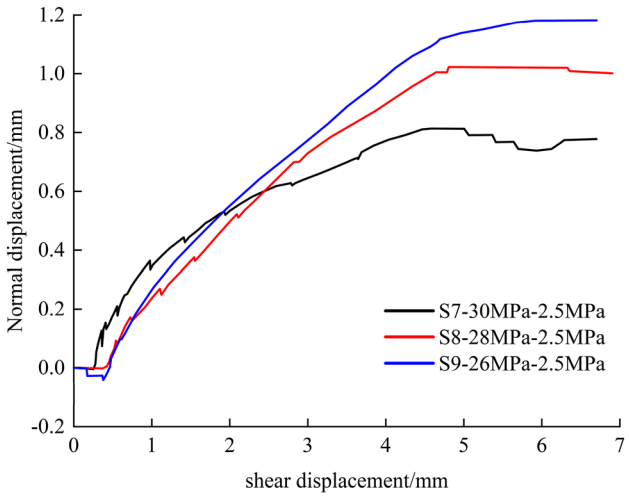

(a) Specimens S7, S8 and S9

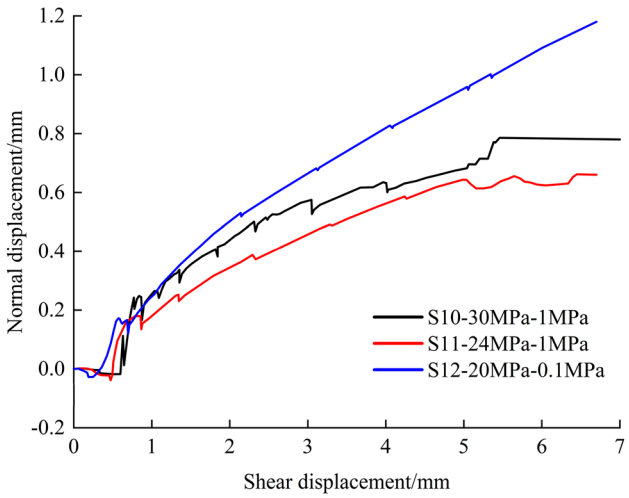

(b) Specimens S10, S11 and S12

Fig. 10 Relationship between normal displacement and shear displacement for rough fractured sandstones

and the viscosity coefficient of water at room temperature is 1.005×10^{-3} Pa· s; w is the fracture width (m); ΔP is the seepage pressure difference at both ends of the specimen (Pa);ΔL is the effective seepage length of the fracture along the seepage direction during the process of shearing slip(m), which can be expressed as:

$$\Delta L = L - U_t \tag{4}$$

In practice, ideal fractures do not exist, and most of the fracture surfaces are rough. Therefore, the mechanical opening in the cubic law is no longer the geometric average fracture width, but the fracture opening obtained by substituting the experimental fracture flow rate into the cubic law, that is, the equivalent hydraulic opening b_h. Therefore, Eq. (3) can be rewritten as (Esaki et al. 1999):

$$Q = \frac{b_h^3 w \Delta P}{12\mu\Delta L} \tag{5}$$

According to Eq. (5), hydraulic opening is:

$$b_h = -\left(\frac{12Q\mu\Delta L}{w\Delta P}\right)^{\frac{1}{3}} \tag{6}$$

Based on the above analysis, the fracture permeability obtained in this test according to Darcy's law is (He et al. 2021):

$$k = \frac{b_h^2}{12} = \frac{1}{2.9}\left(\frac{Q\mu\Delta L}{w\Delta P}\right)^{\frac{2}{3}} \tag{7}$$

The permeability–shear displacement variation curve of the specimen with a rough fracture during shearing is shown in Fig. 13. The permeability variation of different fracture specimens during the shearing process basically conforms to the following law: under a constant normal stress, with increasing shear displacement, fracture permeability will undergo a three-stage change process of "decrease-increase-stability". The "decrease" process in the first stage is primarily caused by the contact closure of the bulge between the fracture surfaces, causing the seepage channel between the fractures to shrink, resulting in a decrease in permeability. In the second stage, fracture permeability will increase significantly with increasing shear displacement, which is primarily caused by the shear dilatation characteristics of the fracture surface. That is to say, the convex contact of the fracture surface will appear to increase with increasing shear displacement, which will lead to an increased fracture opening and permeability. Finally, as shear displacement continues to increase, permeability gradually tends to stabilize. In addition, there are many bumps in the specimen with rough fractures, which produce complex surface geometry, leading to fluctuation of the seepage field even after it is stabilized.

The permeability–shear displacement curve of the smooth fractured sandstone during shearing is shown in Fig. 14. Different from the rough fractured sandstone, the fracture permeability does not shrink in the initial stage of shearing but increases rapidly with increasing shear displacement. In addition, because the roughness of the fracture surface is very small and the distribution of fracture opening is relatively uniform, the permeability change of the sawed sandstone specimens is smaller than that of the rough fractured sandstone specimens.

3.3 Analysis of Permeability Characteristics of Fractured Sandstone Specimens Under Cyclic Loading and Unloading

During the test, the shear stress and seepage pressure were zero when the confining pressure was loaded for the first time. Therefore, this section examines the influence of cyclic loading and unloading on fracture permeability after shear stress and seepage pressure are applied.

The permeability curves of smooth and rough fractured sandstone specimens at various stages are shown in Fig. 15. Confining pressure has an effect on the permeability of smooth and rough fractured sandstone specimens in each stage. With increasing loading and unloading times, the permeability changes of the two types of specimens become more and more intuitive. The unloading stage is the main

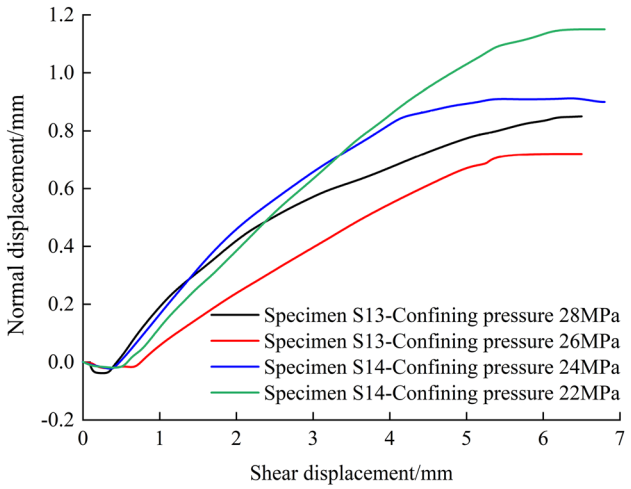

Fig. 11 Relationship between normal displacement and shear displacement for rough fractured sandstones without seepage pressure coupling

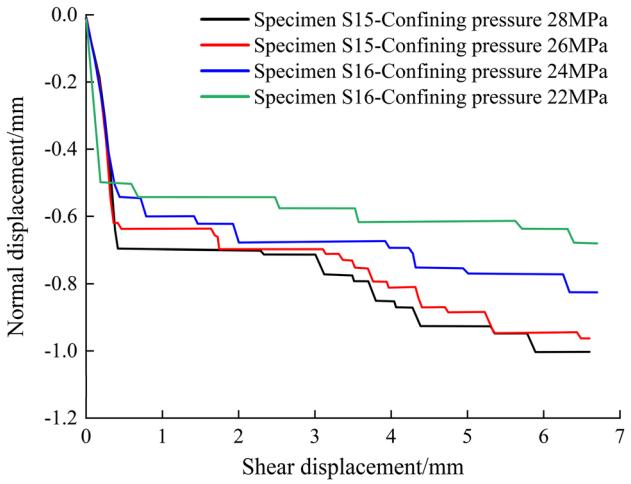

Fig. 12 Relationship between normal displacement and shear displacement for smooth fractured sandstones

stage of permeability variation for the sandstone specimens, and the highest point of permeability of three-cycle loading and unloading appears at the end of the unloading stage.

For the two types of fractured sandstone specimens, permeability decreases during loading, and permeability recovers during unloading, but the recovery values during unloading are all smaller than the permeability values during loading under the same stress conditions (Fig. 15). The deformation of the fractures in the specimen is plastic deformation. A change in confining pressure during loading will cause deformation of the fractures. Although the deformation can be recovered to a certain extent, the fracture permeability cannot be restored to the original value after

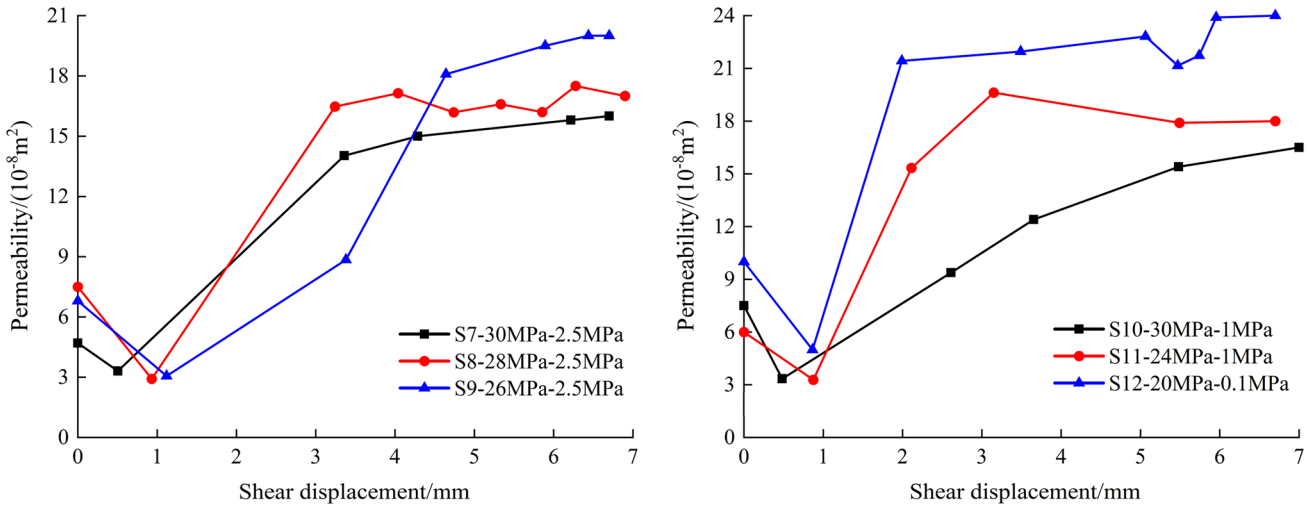

(a) Specimens S7, S8 and S9 **(b)** Specimens S10, S11 and S12

Fig. 13 Relationship between permeability and shear displacement for rough fractured sandstones

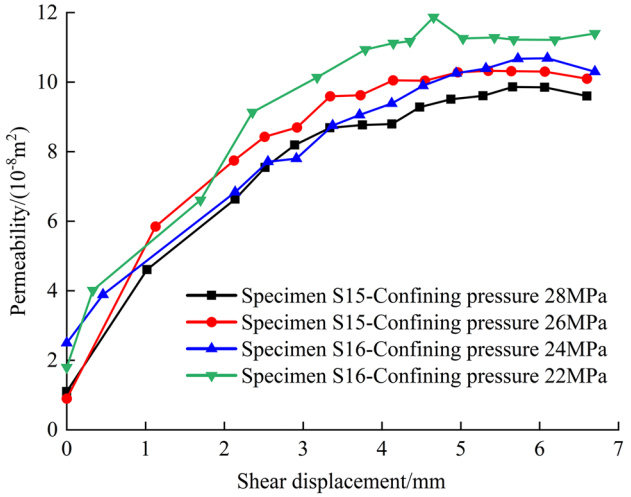

Fig. 14 Relationship between permeability and shear displacement for smooth fractured sandstones

the confining pressure is restored, indicating that the damage caused by confining pressure to the permeability of fractured rock mass is permanent. In addition, at the beginning of each cyclic loading stage, the slope of the change curve of permeability with confining pressure is relatively large, and as confining pressure continues to increase, the slope of the change curve of permeability with confining pressure gradually decreases. At the beginning of the unloading stage in each cycle, the slope of the change curve of permeability with confining pressure is small, and as confining pressure continues to decrease, the slope of the change curve of permeability with confining pressure gradually increases. The initial stage of loading and the late stage of unloading are the primary stages in which the permeability changes, and these two stages are the primary stages in which the sensitivity of the permeability to stress is reflected.

The variation curves of permeability of fractured sandstone specimens under different seepage pressures under cyclic loading and unloading paths are shown in Fig. 16. The greater the seepage pressure, the greater the influence on permeability, because the fracture surface will be deformed under the action of seepage pressure, resulting in permeability change. From the above analysis, both confining pressure and seepage pressure will cause differences in permeability within a fractured rock mass.

According to the fitting analysis of the variation law of permeability with confining pressure during loading and unloading, the permeability and confining pressure have a negative exponential relationship, and the fitting equation is:

$$k = ae^{-b\sigma} + c, \tag{8}$$

where σ is the confining pressure (MPa); a, b, c are fitting parameters.

Fitting parameters of different loading and unloading stages are shown in Table 3.

Both the coefficient a and coefficient c decrease with increasing loading times and unloading times (Table 3). In addition, the coefficient b can reflect the sensitivity of sandstone permeability to stress, that is, the sensitivity of the opening and closing degree of fractures to stress. The loading stage is the sensitivity of the degree of fracture closure to stress, and the coefficient b decreases gradually with increasing loading times, indicating that the sensitivity of

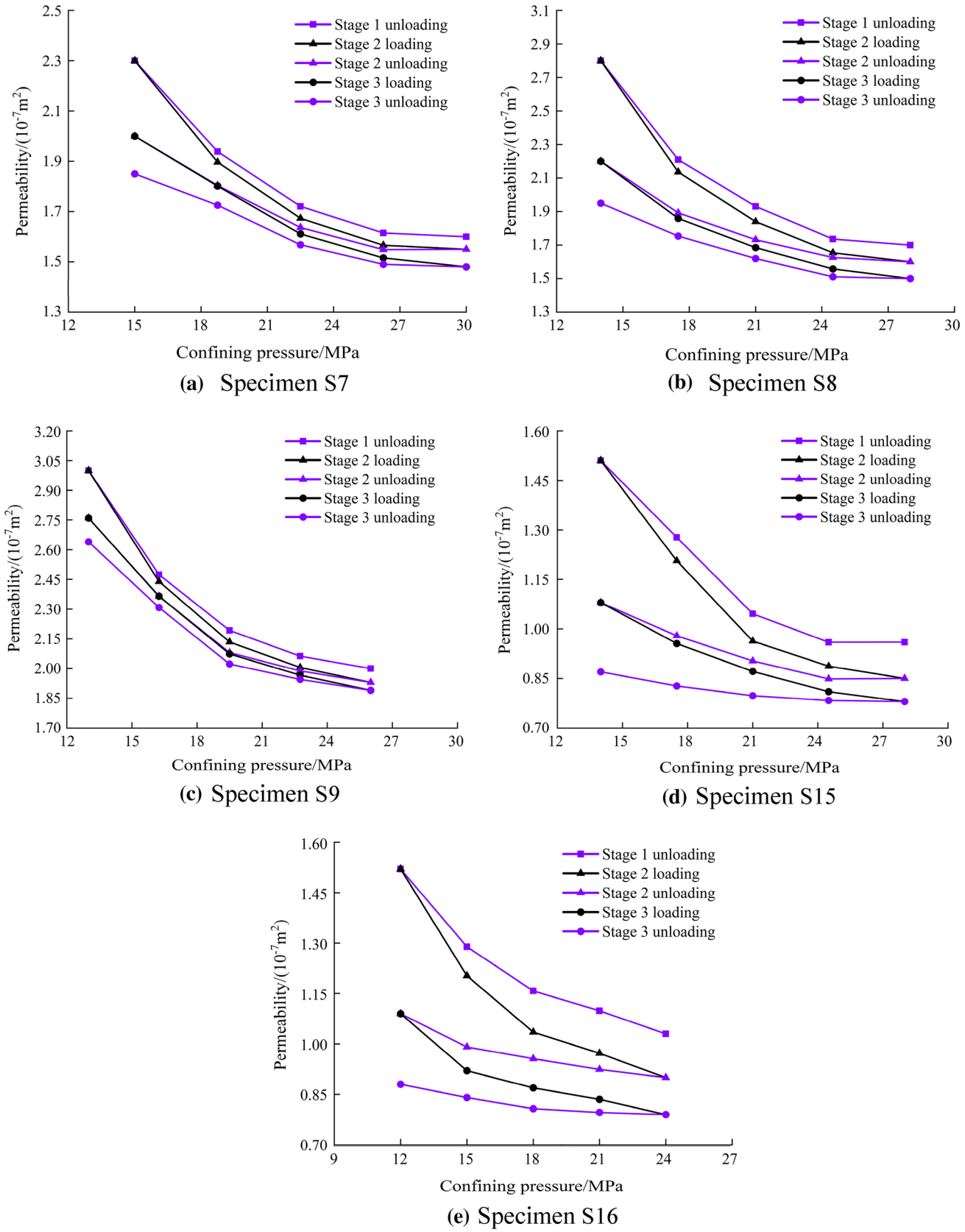

Fig. 15 Permeability variation curve of smooth and rough fractured sandstone specimens under cyclic loading and unloading

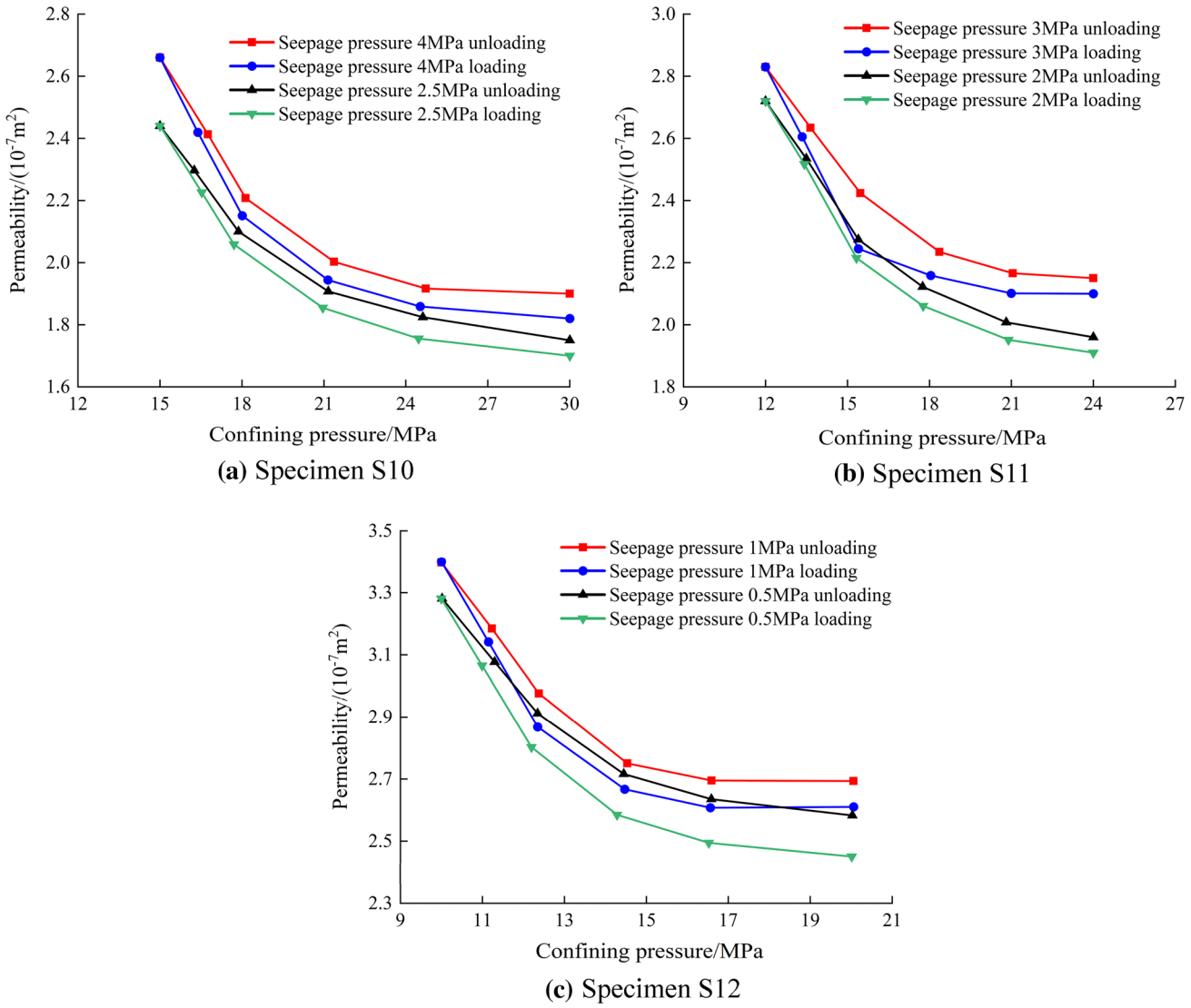

Fig. 16 Permeability variation curve of rough fractured sandstone specimens under different seepage pressures

fractured sandstone specimens to stress gradually decreases with increasing loading time. The unloading stage is the sensitivity of fracture opening to stress, and the coefficient b decreases gradually with increasing unloading times, indicating that the sensitivity of fractured sandstone specimens to stress gradually decreases with increasing unloading times.

4 Conclusions

In this study, the shear-seepage coupling test device and test method of single fractured rock mass were designed by processing specific "double L shaped" specimens, effectively resolving the issue that it is challenging to ensure fluid tightness in the test. At the same time, the shear-seepage coupling test of single fractured sandstone specimens under different confining pressures and seepage pressures was carried out. The test results not only reveal the shear-seepage coupling characteristics of fractured rock mass with different roughness, but also provide important guiding significance for rock mass engineering excavation. The following conclusions can be drawn:

(1) When confining pressure is constant, the influence of seepage pressure on the hydro-mechanical coupling of rough fractures has a threshold value. When the seepage pressure is lower than the threshold value, the characteristics of hydro-mechanical coupling are not significant. When it increases into the threshold value, the coupling characteristics are significant. In addition, when the confining pressure is low, the change in flow

Table 3 Fitting parameter values

Specimen	Loading and unloading process	a	b	c	R^2
S7	Stage 1 unloading	11.6904	0.1812	1.5324	0.9972
	Stage 2 loading	14.7369	0.1931	1.4900	0.9981
	Stage 2 unloading	4.7679	0.1454	1.4683	0.9880
	Stage 3 loading	3.6715	0.1145	1.3478	0.9931
	Stage 3 unloading	2.4620	0.1064	1.3607	0.9799
S8	Stage 1 unloading	17.9716	0.1937	1.6072	0.9985
	Stage 2 loading	22.9744	0.2065	1.5237	0.9994
	Stage 2 unloading	8.2569	0.1803	1.5395	0.9989
	Stage 3 loading	7.0725	0.1569	1.4119	0.9994
	Stage 3 unloading	3.6788	0.1356	1.4027	0.9935
S9	Stage 1 unloading	16.7444	0.2113	1.9277	0.9999
	Stage 2 loading	17.9627	0.2117	1.8559	0.9997
	Stage 2 unloading	11.0637	0.1912	1.8440	0.9966
	Stage 3 loading	9.2387	0.1720	1.7785	0.9973
	Stage 3 unloading	8.6097	0.1776	1.7928	0.9923
S15	Stage 1 unloading	6.2408	0.1608	0.8636	0.9825
	Stage 2 loading	8.3481	0.1724	0.7697	0.9936
	Stage 2 unloading	2.1551	0.1459	0.8034	0.9892
	Stage 3 loading	1.9278	0.1166	0.7037	0.9995
	Stage 3 unloading	1.1029	0.1699	0.7684	0.9966
S16	Stage 1 unloading	4.6402	0.1788	0.9753	0.9978
	Stage 2 loading	8.8298	0.2164	0.8613	0.9982
	Stage 2 unloading	2.0260	0.1916	0.8845	0.9926
	Stage 3 loading	5.0885	0.2357	0.7858	0.9876
	Stage 3 unloading	0.9601	0.1854	0.7772	0.9939

rate with seepage pressure can be fit to the data using an exponential function; when the confining pressure is high, the change in flow rate with seepage pressure can be fit to the data using a bilinear function.

(2) The peak shear stress, residual shear stress, and shear stiffness of rough fractures all increase with increasing confining pressure, while the change in normal dilatation displacement is the opposite. In addition, different from rough fractured sandstone specimens, smooth fractured specimens do not soften immediately after reaching the shear stress peak but continue to fluctuate slowly within a 1 MPa range. And the smooth fracture specimens are in shear shrinkage state, with the normal shrinkage displacement of less than 1.0 mm. The curves of shear stress and normal displacement of specimens without seepage pressure coupling have the same variation trend as those of specimens with shear-seepage coupling; however, there are no periodic drops and fluctuations in the late shearing period.

(3) Under a constant normal stress, with increasing shear displacement, the permeability of rough fractures changes in the staged manner of "decrease-increase-stability", which is closely related to the mechanical properties of asperities on the fracture surface. Different from rough fractured sandstone, the permeability of the smooth fractured specimens does not decrease as described above but increases rapidly with increasing shear displacement.

(4) During cyclic loading and unloading, the permeability in the loading stage decreases with increasing confining pressure, and permeability in the unloading stage increases with decreasing confining pressure. During unloading, permeability recovered to some extent but could not return to the original value, indicating that the damage caused by the confining pressure to the permeability of the fractured rock mass was permanent. In addition, the initial stage of loading and later stage of unloading are the primary stages of permeability change of fractured sandstone specimens. Under cyclic loading and unloading, permeability and confining pressure have a negative exponential function.

Acknowledgements This work was supported by the National Natural Science Foundation of China (Grant No.U1602232), the Liaoning Province Science and technology plan, China (2019JH2-10100035), the Fundamental Research Funds for the Central Universities (N170108029), the fundamental research funds for the central universities (Grant No.2101018), Study on dynamic characterization method and catastrophe criterion of surrounding rock damage under large-scale mining in deep multi-mining area (SMDPC202103) and the China Scholarship Council (CSC No.201906080071) for a joint Ph.D. fellowship, which enabled Tianjiao Yang to visit the Environmental Geomechanics Laboratory, the Department of Civil Engineering and Applied Mechanics, McGill University, Canada.

Author Contributions TY: conceptualization, methodology, experiment, software, visualization, writing—original draft. PW: data curation, experiment, investigation, writing—review and editing, funding acquisition. SW: supervision, formal analysis, funding acquisition. HL: experiment, writing—review and editing. ZZ: experiment, writing—review and editing.

Declarations

Conflict of Interest The authors declare that they have no known competing financial interests or personal relationships that could have appeared to influence the work reported in this paper.

References

Aalianvari A (2017) Combination of engineering geological data and numerical modeling results to classify the tunnel route based on the groundwater seepage. Geomech Eng 13(4):671–683. https://doi.org/10.12989/gae.2017.13.4.671

Abierdi XYZ, Zhong HY, Gu X, Liu HL, Zhang WG (2020) Laboratory model tests and DEM simulations of unloading-induced tunnel failure mechanism. CMC-Comput Mater Con 63(2):825–844. https://doi.org/10.3264/cmc.2020.07946

Ahola MP, Mohanty S, Makurat A (1996) Coupled mechanical shear and hydraulic flow behavior of natural rock joints. Dev Geotech Eng 79(C):393–423. https://doi.org/10.1016/S0165-1250(96)80034-4

Boulon MJ, Selvadurai APS, Benjelloun H, Feuga B (1993) Influence of rock joint degradation on hydraulic conductivity. Int J Rock Mech Min Sci Geomech Abstr 30(7):1311–1317. https://doi.org/10.1016/0148-9062(93)90115-T

Cao C, Xu ZG, Chai JR, Qin Y, Tan R (2018) Mechanical and hydraulic behaviors in a single fracture with asperities crushed during shear. Int J Geomech 18(11):04018148. https://doi.org/10.1061/(ASCE)GM.1943-5622.0001277

Cappa F, Guglielmi Y, Rutqvist J, Tsang CF, Thoraval A (2005) Hydromechanical interactions in a fractured carbonate reservoir inferred from hydraulic and mechanical measurements. Int J Rock Mech Min 42(2):287–306. https://doi.org/10.1016/j.ijrmms.2004.11.006

Cappa F, Guglielmi Y, Rutqvist J, Tsang CF, Thoraval A (2006) Hydromechanical modelling of pulse tests that measure fluid pressure and fracture normal displacement at the Coaraze laboratory site. France Int J Rock Mech Min 43(7):1062–1082. https://doi.org/10.1016/j.ijrmms.2006.03.006

Chao ZM, Ma GT, Hu XW, He K, Luo G, Mei XF, Li D (2020) Experimental research on stress-dependent permeability and porosity of rock-like materials with different thicknesses of smooth hidden joints. Int J Mod Phys B 34(12):2050117. https://doi.org/10.1142/S0217979220501179

Chen Z, Narayan SP, Yang Z, Rahman SS (2000) An experimental investigation of hydraulic behaviour of fractures and joints in granitic rock. Int J Rock Mech Min 37(7):1061–1071. https://doi.org/10.1016/S1365-1609(00)00039-3

Chen HM, Zhao ZY, Choo LQ, Sun JP (2016) Rock cavern stability analysis under different hydro-geological conditions using the coupled hydro-mechanical model. Rock Mech Rock Eng 49(2):555–572. https://doi.org/10.1007/s00603-015-0748-4

Chen SJ, Feng F, Wang YJ, Li DY, Huang WP, Zhao XD, Jiang N (2020) Tunnel failure in hard rock with multiple weak planes due to excavation unloading of in-situ stress. J Cent South Univ 27(10):2864–2882. https://doi.org/10.1007/s11771-020-4515-7

Di ST, Jia C, Qiao WG, Yu WJ, Li K (2017) Theoretical and experimental investigation of characteristics of single fracture stress-seepage coupling considering microroughness. Math Probl Eng. https://doi.org/10.1155/2017/6431690

Duan K, Ji YL, Wu W, Kwok CY (2019) Unloading-induced failure of brittle rock and implications for excavation induced strain burst. Tunn Undergr Sp Tech 84(2):495–506. https://doi.org/10.1016/j.tust.2018.11.012

Eggertsson GH, Lavallee Y, Kendrick JE, Markusson SH (2020) Improving fluid flow in geothermal reservoirs by thermal and mechanical stimulation: the case of Krafla volcano. Iceland J Volcanol Geoth Res 391:106351. https://doi.org/10.1016/j.jvolgeores.2018.04.008

Esaki T, Du S, Mitani Y, Ikusada K, Jing L (1999) Development of a shear-flow test apparatus and determination of coupled properties for a single rock joint. Int J Rock Mech Min 36(5):641–650. https://doi.org/10.1016/S0148-9062(99)00044-3

Faoro I, Vinciguerra S, Marone C, Elsworth D, Schubnel A (2013) Linking permeability to crack density evolution in thermally stressed rocks under cyclic loading. Geophys Res Lett 40(11):2590–2595. https://doi.org/10.1002/grl.50436

Feng F, Chen SJ, Li DY, Huang WP, Peng K, Zang CW (2020) Excavation unloading-induced fracturing of hard rock containing different shapes of central holes affected by unloading rates and in situ stresses. Energy Sci Eng 8(1):4–27. https://doi.org/10.1002/ese3.486

Fu CH, Xie HP, Gao MZ, Wang F, Xie J, Liu JJ, Yang BG, Tang RF (2021) Mechanical behaviour and seepage characteristics of coal under the loading path of roadway excavation and coal mining. Geomat Nat Haz Risk 12(1):1862–1884. https://doi.org/10.1080/19475705.2021.1948451

Gramiger LM, Moore JR, Gischig VS, Loew S, Funk M, Limpach P (2020) Hydromechanical rock slope damage during late pleistocene and holocene glacial cycles in an alpine valley. J Geophys Res-Earth. https://doi.org/10.1029/2019JF005494

Gui Y, Xia CC, Ding WQ, Qian X, Du SG (2017) A new method for 3D modeling of joint surface degradation and void space evolution under normal and shear loads. Rock Mech Rock Eng 50(10):2827–2836. https://doi.org/10.1007/s00603-017-1242-y

Guo JQ, Qian Y, Chen JX, Chen F (2019) The minimum safe thickness and catastrophe process for water inrush of a karst tunnel face with multi fractures. Processes 7(10):686. https://doi.org/10.3390/pr7100686

He XP, Sinan M, Kwak H, Hoteit H (2021) A corrected cubic law for single-phase laminar flow through rough-walled fractures. Adv Water Resour 154:103984. https://doi.org/10.1016/j.advwatres.2021.103984

Huang N, Jiang YJ, Liu RC, Li B, Zhang ZY (2017) A predictive model of permeability for fractal-based rough rock fractures during shear. Fractals 25(5):1750051. https://doi.org/10.1142/S0218348X17500517

Huang MQ, Zhang L, Zhang C, Cheng S (2020) Characteristics of permeability changes in bituminous coal under conditions of stress variation due to repeated mining activities. Nat Resour Res 29(3):1687–1704. https://doi.org/10.1007/s11053-019-09542-0

Jang HS, Kang SS, Jang BA (2014) Determination of joint roughness coefficients using roughness parameters. Rock Mech Rock Eng 47(6):2061–2073. https://doi.org/10.1007/s00603-013-0535-z

Javadi M, Sharifzadeh M, Shahriar K, Mitani Y (2014) Critical reynolds number for nonlinear flow through rough-walled fractures: the role of shear processes. Water Resour Res 50(2):1789–1804. https://doi.org/10.1002/2013WR014610

Jia P, Yang N, Liu DQ (2021) Effect of unloading direction on rock failure under true triaxial stress conditions. J Test Eval 49(6):4058–4071. https://doi.org/10.1520/JTE20200298

Jiang Q, Zhang MZ, Yan F, Su GS, Feng XT, Xu DP, Feng GL (2020) Effect of initial minimum principal stress and unloading rate on the spalling and rockburst of marble: a true triaxial experiment investigation. B Eng Geol Environ 80(2):1617–1634. https://doi.org/10.1007/s10064-020-01995-5

Kling T, Huo D, Schwarz JO, Enzmann F, Benson S, Blum P (2016) Simulating stress-dependent fluid flow in a fractured core sample using real-time X-ray CT data. Solid Earth 7(4):1109–1124. https://doi.org/10.5194/se-7-1109-2016

Kong HL, Yin MG, Wang LZ, Zhang HL, Ji F (2021) A review of the mass-loss-induced non-Darcy seepage and seepage suffosion in the fractured zone: the concepts discrimination and connection. Arab J Geosci 14(23):2522. https://doi.org/10.1007/s12517-021-08754-0

Koyama T, Li B, Jiang Y, Jing L (2009) Numerical modelling of fluid flow tests in a rock fracture with a special algorithm for contact areas. Comput Geotech 36(1–2):291–303. https://doi.org/10.1016/j.compgeo.2008.02.010

Lee HS, Cho TF (2002) Hydraulic characteristics of rough fractures in linear flow under normal and shear load. Rock Mech Rock Eng 35(4):299–318. https://doi.org/10.1007/s00603-002-0028-y

Li XB, Du K, Li DY (2015) True triaxial strength and failure modes of cubic rock specimens with unloading the minor principal stress. Rock Mech Rock Eng 48(6):2185–2196. https://doi.org/10.1007/s00603-014-0701-y

Li B, Liu RC, Jiang YJ (2019) An experimental method to visualize shear-induced channelization of fluid flow in a rough-walled fracture. Hydrogeol J 27(8):3097–3106. https://doi.org/10.1007/s10040-019-02048-2

Li LP, Tu WF, Zhou ZQ, Shi SH, Zhang MG, Chen YX (2020) Dynamic unloading instability mechanism of underground cavern based on seepage-damage coupling. KSCE J Civ Eng 24(5):1620–1631. https://doi.org/10.1007/s12205-020-1288-3

Li JB, Wang YH, Tan ZS, Du W, Liu ZY (2021) Study on water inflow variation law of no.1 shaft auxiliary shaft in highligongshan based on dual medium model. Symmetry-Basel 13(6):930. https://doi.org/10.3390/sym13060930

Liu W, Chen YF, Hu R, Zhou W, Zhou CB (2016) A two-step homogenization-based permeability model for deformable fractured rocks with consideration of coupled damage and friction effects. Int J Rock Mech Min 89:212–226. https://doi.org/10.1016/j.ijrmms.2016.09.009

Liu C, Yu BC, Zhang DM, Zhao HG (2020a) Experimental study on strain behavior and permeability evolution of sandstone under constant amplitude cyclic loading-unloading. Energy Sci Eng. https://doi.org/10.1002/ese3.527

Liu RC, Huang N, Jiang YJ, Han GS, Jing HW (2020b) Effect of shear direction change on shear-flow-transport processes in single rough-walled rock fractures. Transport Porous Med 133(3):373–395. https://doi.org/10.1007/s11242-020-01428-7

Liu J, Li ZP, Zhang X, Weng XJ (2021) Analysis of water and mud inrush in tunnel fault fracture zone-a case study of Yonglian tunnel. Sustainability-Basel 13(17):9585. https://doi.org/10.3390/su13179585

Ma YQ, Zhang YJ, Huang YB, Zhang Y, Hu ZJ (2019) Experimental study on flow and heat transfer characteristics of water flowing through a rock fracture induced by hydraulic fracturing for an enhanced geothermal system. Appl Therm Eng 154:433–441. https://doi.org/10.1016/j.applthermaleng.2019.03.114

Meng QB, Zhang MW, Han LJ, Pu H, Nie TY (2016) Effects of acoustic emission and energy evolution of rock specimens under the uniaxial cyclic loading and unloading compression. Rock Mech Rock Eng 49(10):3873–3886. https://doi.org/10.1007/s00603-016-1077-y

Meng QB, Zhang MW, Han LJ, Pu H, Chen YL (2018) Acoustic emission characteristics of red sandstone specimens under uniaxial cyclic loading and unloading compression. Rock Mech Rock Eng 51(4):969–988. https://doi.org/10.1007/s00603-017-1389-6

Mofakham AA, Stadelman M, Ahmadi G, Shanley KT, Crandall D (2018) Computational modeling of hydraulic properties of a sheared single rock fracture. Transport Porous Med 124(1):1–30. https://doi.org/10.1007/s11242-018-1030-5

Nishiyama S, Ohnishi Y, Ito H, Yano T (2014) Mechanical and hydraulic behavior of a rock fracture under shear deformation. Earth Planets Space 66:108. https://doi.org/10.1186/1880-5981-66-108

Olsson R, Barton N (2001) An improved model for hydromechanical coupling during shearing of rock joints. Int J Rock Mech Min 38(3):317–329. https://doi.org/10.1016/S1365-1609(00)00079-4

Park H, Osada M, Matsushita T, Takahashi M, Ito K (2013) Development of coupled shear-flow-visualization apparatus and data analysis. Int J Rock Mech Min 63:72–81. https://doi.org/10.1016/j.ijrmms.2013.06.003

Peguiron F, Labiouse V (2020) Consideration of anisotropies related to bedding planes in the modelling of thick-walled hollow cylinder tests on boom clay. Eur J Environ Civ En. https://doi.org/10.1080/19648189.2020.1830178

Qian X, Xia CC, Gui Y (2018) Quantitative estimates of non-darcy groundwater flow properties and normalized hydraulic aperture through discrete open rough-walled joints. Int J Geomech 18(9):04018099. https://doi.org/10.1061/(ASCE)GM.1943-5622.0001228

Qiu SL, Feng XT, Xiao JQ, Zhang CQ (2014) An experimental study on the pre-peak unloading damage evolution of marble. Rock Mech Rock Eng 47(2):401–419. https://doi.org/10.1007/s00603-013-0394-7

Ren JX, Chen X, Chen XZ, Yun MC, Cao XT, Liu TT (2020) Effect of porewater pressure on the mechanical properties of red sandstone with different unloading rates. Q J Eng Geol Hydroge. https://doi.org/10.1144/qjegh2019-101

Rong G, Yang J, Cheng L, Zhou CB (2016) Laboratory investigation of nonlinear flow characteristics in rough fractures during shear process. J Hydrol 541:1385–1394. https://doi.org/10.1016/j.jhydrol.2016.08.043

Rong G, Yang J, Cheng L, Tan J, Peng J, Zhou CB (2018) A forchheimer equation-based flow model for fluid flow through rock fracture during shear. Rock Mech Rock Eng 51(9):2777–2790. https://doi.org/10.1007/s00603-018-1497-y

Sathar S, Reeves HJ, Cuss RJ, Harrington JF (2012) The role of stress history on the flow of fluids through fractures. Mineral Mag 76(8):3165–3177. https://doi.org/10.1180/minmag.2012.076.8.30

Shen N, Li XC, Zhang Q, Wang L (2021) Comparison of shear-induced gas transmissivity of tensile fractures in sandstone and shale under varying effective normal stresses. J Nat Gas Sci Eng 95:104218. https://doi.org/10.1016/j.jngse.2021.104218

Sun WB, Xue YC, Yin LM, Zhang JM (2019) Experimental study on seepage characteristics of large size rock specimens under three-dimensional stress. Geomech Eng 18(6):567–574. https://doi.org/10.12989/gae.2019.18.6.567

Tian ZX, Dai CQ, Zhao QS, Meng ZB, Zhang BL (2021) Experimental study of join roughness influence on fractured rock mass seepage. Geofluids. https://doi.org/10.1155/2021/8813743

Tse R, Cruden DM (1979) Estimating joint roughness coefficients. Int J Rock Mech Min Sci Geomech Abstr 16(5):303–307. https://doi.org/10.1016/0148-9062(79)90241-9

Vazaios I, Vlachopoulos N, Diederichs MS (2019) Assessing fracturing mechanisms and evolution of excavation damaged zone of tunnels in interlocked rock masses at high stresses using a finite-discrete element approach. J Rock Mech Geotech Eng 11(4):701–722. https://doi.org/10.1016/j.jrmge.2019.02.004

Vogler D, Amann F, Bayer P, Elsworth D (2016) Permeability evolution in natural fractures subject to cyclic loading and gouge formation. Rock Mech Rock Eng 49(9):3463–3479. https://doi.org/10.1007/s00603-016-1022-0

Wang CS, Jiang YJ, Liu RC, Wang C, Zhang ZY, Sugimoto S (2020a) Experimental study of the nonlinear flow characteristics of fluid in 3d rough-walled fractures during shear process. Rock Mech Rock Eng 53(6):2581–2604. https://doi.org/10.1007/s00603-020-02068-5

Wang M, Guo QF, Shan PF, Cai MF, Ren FH, Dai B (2020b) Numerical research of fluid flow and solute transport in rough fractures under different normal stress. Geofluids 3:1–17. https://doi.org/10.1155/2020/8845216

Wu ZJ, Fan LF, Zhao SH (2018) Effects of hydraulic gradient, intersecting angle, aperture, and fracture length on the nonlinearity of fluid flow in smooth intersecting fractures: an experimental investigation. Geofluids. https://doi.org/10.1155/2018/9352608

Xiang YZ, Zeng ZK, Xiang YJ, Abi E, Zheng YR, Yuan HC (2021) Tunnel failure mechanism during loading and unloading processes through physical model testing and DEM simulation. Sci Rep-UK 11(1):16753. https://doi.org/10.1038/s41598-021-96206-w

Xiong XB, Li B, Jiang YJ, Koyama T, Zhang CH (2011) Experimental and numerical study of the geometrical and hydraulic characteristics of a single rock fracture during shear. Int J Rock Mech Min 48(8):1292–1302. https://doi.org/10.1016/j.ijrmms.2011.09.009

Xue Y, Liu Y, Dang FN, Liu J, Ma ZY, Zhu L, Yang HW (2019) Assessment of the nonlinear flow characteristic of water inrush based on the brinkman and forchheimer seepage model. Water-Sui 11(4):855. https://doi.org/10.3390/w11040855

Yang TJ, Wang SH, Wang PY, Zhang Z (2021) Hydraulic and mechanical coupling analysis of rough fracture network under normal

stress and shear stress. KSCE J Civ Eng. https://doi.org/10.1007/s12205-021-0660-2

Yeo IW, De Freitas MH, Zimmerman RW (1998) Effect of shear displacement on the aperture and permeability of a rock fracture. Int J Rock Mech Min 35(8):1051–1070. https://doi.org/10.1016/S0148-9062(98)00165-X

Yin Q, Ma GW, Jing HW, Wang HD, Su HJ, Wang YC, Liu RC (2017) Hydraulic properties of 3D rough-walled fractures during shearing: an experimental study. J Hydrol 555:169–184. https://doi.org/10.1016/j.jhydrol.2017.10.019

Zhang C, Zhang L, Zhao YX, Wang W (2018) Experimental study of stress-permeability behavior of single persistent fractured coal samples in the fractured zone. J Geophys Eng 15(5):2159. https://doi.org/10.1088/1742-2140/aac12e

Zhang X, Chai JR, Qin Y, Cao J, Cao C (2019) Experimental study on seepage and stress of single-fracture radiation flow. KSCE J Civ Eng 23(3):1132–1140. https://doi.org/10.1007/s12205-019-1519-7

Zhang T, Liu Y, Yang K, Tang M, Yu X, Yu F (2020) Hydromechanical coupling characteristics of the fractured sandstone under cyclic loading-unloading. Geofluids 2:1–12. https://doi.org/10.1155/2020/8811003

Zhang HW, Wan ZJ, Zhao YX, Zhang Y, Chen YL, Wang JH, Cheng JY (2021a) Shear induced seepage and heat transfer evolution in a single-fractured hot-dry-rock. Cmes-Comp Model Eng 126(2):443–455. https://doi.org/10.32604/cmes.2021a.013179

Zhang L, Huang MQ, Li MX, Lu S, Yuan XC, Li JH (2021b) Experimental study on evolution of fracture network and permeability characteristics of bituminous coal under repeated mining effect. Nat Resour Res. https://doi.org/10.1007/s11053-021-09971-w

Zhang T, Xu WY, Wang HL, Wang RB, Yan L, Hu MT (2021c) Anisotropic mechanical behaviour of columnar jointed rock masses subjected to cyclic loading: an experimental investigation. Int J Rock Mech Min 148:104954. https://doi.org/10.1016/j.ijrmms.2021.104954

Zhao LH, Zhang SH, Huang DL, Zuo S, Li DJ (2018) Quantitative characterization of joint roughness based on semivariogram parameters. Int J Rock Mech Min 109:1–8. https://doi.org/10.1016/j.ijrmms.2018.06.008

Zhao K, Wang QZ, Chen Q, Zhuang HY, Chen GX (2021a) Simplified effective stress modeling of shear wave propagation in saturated granular soils. Geotech Lett 11(1):1–9. https://doi.org/10.1680/jgele.19.00023

Zhao Y, Bi J, Wang CL, Liu P (2021b) Effect of unloading rate on the mechanical behavior and fracture characteristics of sandstones under complex triaxial stress conditions. Rock Mech Rock Eng 54(9):4851–4866. https://doi.org/10.1007/s00603-021-02515-x

Zhao K, Wang QZ, Zhuang HY, Li ZY, Chen GX (2022) A fully coupled flow deformation model for seismic site response analyses of liquefiable marine sediments. Ocean Eng 251:111144. https://doi.org/10.1016/j.oceaneng.2022.111144

Zhou XP, Shou YD (2013) Excavation-induced zonal disintegration of the surrounding rock around a deep circular tunnel considering unloading effect. Int J Rock Mech Min 64:246–257. https://doi.org/10.1016/j.ijrmms.2013.08.010

Zhu GA, Dou LM, Wang CB, Ding ZW, Feng ZJ, Xue F (2019) Experimental study of rock burst in coal samples under overstress and true-triaxial unloading through passive velocity tomography. Safety Sci 117:388–403. https://doi.org/10.1016/j.ssci.2019.04.012